

# Evolution mechanism of mesoporous silicon nanopillars grown by metal-assisted chemical etching and nanosphere lithography: correlation of Raman spectra and red photoluminescence

Prajith Karadan<sup>1,2</sup> · Siju John<sup>1</sup> · Aji A. Anappara<sup>2</sup> · Chandrabhas Narayana<sup>3</sup> · Harish C. Barshilia<sup>1</sup>

Received: 8 March 2016 / Accepted: 8 June 2016 / Published online: 18 June 2016  
© Springer-Verlag Berlin Heidelberg 2016

**Abstract** We have fabricated highly ordered, vertically aligned, high aspect ratio silicon nanopillars (SiNPLs) of diameter  $\sim 80$  nm by combining metal-assisted chemical etching and nanosphere lithography. The evolution of surface morphology of porous silicon nanopillars has been explained, and the presence of mesoporous structures was detected on the top of silicon nanopillars using field emission scanning electron microscopy. The mesoporosity of the SiNPLs is confirmed by Brunauer–Emmett–Teller measurements. The peak shift and the splitting of optical phonon modes into LO and TO modes in the micro-Raman spectra of mesoporous SiNPLs manifest the presence of 2–3 nm porous Si nanocrystallites (*P*-SiNCs) on the top of SiNPLs and the size of crystallites was calculated using bond polarizability model for spherical phonon confinement. The origin of red luminescence is explained using quantum confinement (QC) and QC luminescent center models for the *P*-SiNCs, which is correlated with the micro-Raman spectra. Finally, we confirmed the origin of the red luminescence is from the *P*-SiNCs formed on surface of SiNPLs, highly desired for LED devices by suitably tailoring the substrate.

## 1 Introduction

Silicon nanostructures, including nanowires and nanopillars, are one of the most promising materials for applications in nanoscale electronics [1, 2], photovoltaics and energy conversion [3–5], energy storage [6], optoelectronics [7, 8], nanocapacitor arrays [9], biosensors [10, 11], to name a few. Several studies on silicon nanostructures have been well documented over the last decade [12]. Among the various nanostructures, silicon nanopillars (SiNPLs) have received a lot of attention because of their unique physical, chemical and optical properties [13]. It has been established that SiNPLs have several advantages over the other nanostructures such as strong carrier confinement [14], possibility of tuning of band gap ranging from 0.9 to 4 eV [15], enhanced light trapping and absorption [16], efficient carrier transport [17] and their ability to use the surface for further design parameters [18].

The important challenges in the fabrication of nanopillars are the precise control of the diameter, length, packing density, orientation and uniformity. Silicon nanowires/nanopillars have been fabricated by various methods such as vapor–liquid–solid growth [19, 20], chemical vapor deposition [21, 22], electrochemical etching [23], metal-assisted chemical etching [12, 24] and dry etching methods such as reactive ion etching and inductive coupled plasma process [25, 26]. It is worth pointing out that low-cost and room-temperature methods are desired for wafer scale fabrication, since the reports on novel strategies of various devices based on SiNPLs are increasing day by day. Among these fabrication methods, metal-assisted chemical etching is a facile and low-cost method for fabricating various Si nanostructures with the ability to control various parameters such as diameter, length, orientation, cross-sectional shape and packing density

✉ Harish C. Barshilia  
harish@nal.res.in

<sup>1</sup> Nanomaterials Research Laboratory, Surface Engineering Division, CSIR-National Aerospace Laboratories, Bangalore 560017, India

<sup>2</sup> Department of Physics, National Institute of Technology, Calicut 673601, India

<sup>3</sup> Light Scattering Laboratory, Chemistry and Physics of Materials Unit, Jawaharlal Nehru Centre for Advanced Scientific Research, Bangalore 560064, India

[27–31]. In metal-assisted etching, the whole process occurs at room temperature which avoids the metal diffusion.

Metal-assisted etching in combination with various film patterning techniques has been demonstrated successfully to fabricate SiNPLs with features ranging from several microns to sub 10 nm [32]. In order to get the nanoporous metal film prior to metal-assisted etching, high-cost lithographic techniques such as interference lithography [12] and deep ultraviolet lithography [33] are required. Currently, other complex lithographic techniques have been completely superseded by the nanosphere lithography due to its low-cost and easy assembling. The combined procedure of metal-assisted etching and nanosphere lithography [24, 34–36] is drawing a great deal of interest on account of their ability to fabricate large area aligned Si nanostructures. Polystyrene (PS) nanosphere templates have been used for the semiconductor etching process which controls the diameter and the separation of the SiNPLs.

In this work, we present vertical, high aspect ratio mesoporous SiNPLs of diameters 80 nm, using a facile, room-temperature fabrication technique with controlled length, diameter and interpillar separation. The evolution of porous structures on the top of SiNPLs is discussed in detail, which is confirmed using field emission scanning electron microscopy (FESEM) and Brunauer–Emmett–Teller (BET) measurements. The role of  $\text{H}_2\text{O}_2$  in the formation of porous structure on SiNPLs has been studied using FESEM. The size of the porous Si nanocrystallites was calculated using bond polarizability model for spherical confinement from the Raman spectra. An efficient red emission could be seen for the mesoporous SiNPLs due to the presence of porous Si nanocrystals of size 2–3 nm. The red luminescence is explained using quantum confinement (QC) and quantum confinement luminescent center (QCLC) models for SiNPLs and successfully correlated with Raman spectra. Finally, we conclude that the red emission in our SiNPLs is not due to the QCLC effect but due to the quantum confinement (QC) property of the P-SiNCs.

## 2 Experimental details

### 2.1 Fabrication of silicon nanopillars

The schematic diagram of the entire fabrication process of silicon nanopillars (SiNPLs) is shown in Fig. 1. Silicon wafer with (100) orientation was cut into  $1 \times 1 \text{ cm}^2$  pieces, ultrasonicated with acetone and isopropyl alcohol (IPA) for 15 min each to remove the organic contaminations. To make the wafer hydrophilic in nature, Si wafers have been heated in boiling piranha solution (4:1 (v/v)  $\text{H}_2\text{SO}_4$ :  $\text{H}_2\text{O}_2$ ) at 80 °C for 1 h followed by RCA solution

(1:1:5 (v/v/v)  $\text{NH}_4\text{OH}$ :  $\text{H}_2\text{O}_2$ :  $\text{H}_2\text{O}$ ) for 1 h. Wafers were rinsed with DI water, dried with  $\text{N}_2$  and then heated at 150 °C to remove the water content. Monolayer of PS nanosphere was obtained by spin coating technique. PS spheres of diameter 90 nm, as 10 % by weight in solution, were used in this fabrication process. The PS nanospheres were diluted in ethanol by volume ratio 1:1, and a volume of 20  $\mu\text{L}$  was dropped on the Si substrates placed on a spin coater. Spin coating of PS nanosphere has been conducted in three steps: (1) 200 rpm for 20 s, (2) 1000 rpm for 20 s and (3) 8000 rpm for 60 s. The first step was applied to spread the PS nanospheres on Si surface. The second step was utilized to spin away the excess PS solution and the third step with higher rotation speed was used to get a uniform monolayer of PS nanospheres on the silicon surface. The PS nanospheres were self-assembled in hexagonal close packed structure on the silicon surface.  $\text{O}_2$  plasma etching has been performed in reactive unbalanced magnetron sputtering system to control the size of PS nanospheres. The diameter and the interparticle distance were tailored by varying the  $\text{O}_2$  plasma etching time from 1 to 4 min with constant  $\text{O}_2$  flow rate of 12 sccm, DC bias of  $-500 \text{ V}$  and pressure of 2.8 Pa. Gold thin film of thickness 10 nm was deposited on the  $\text{O}_2$  plasma etched PS nanospheres by sputtering. After gold deposition, the PS nanospheres were removed by ultrasonication in  $\text{CH}_2\text{Cl}_2$  for 30 min. This step can be performed after etching also. When the etching time is more, the PS surface becomes rough and the gold will be coated on the PS nanospheres. Then it is difficult to dissolve the PS nanospheres in  $\text{CH}_2\text{Cl}_2$ . Therefore, after gold thin film deposition, metal-assisted chemical etching can be performed to avoid this problem (shown in Fig. 1). Si substrate with porous gold film was immersed in an etching solution containing HF,  $\text{H}_2\text{O}_2$  and ethanol at room temperature. The etching solution was prepared by HF (40 %),  $\text{H}_2\text{O}_2$  (30 %) and ethanol with volume ratio 3:1:1, respectively. The etching process was observed by the bubble formation and the change in color. Finally, the samples were rinsed with DI water several times and the gold film was removed in aqua regia (3:1 (v/v)  $\text{HCl}$ :  $\text{HNO}_3$ ). Subsequently, the samples were cleaned in DI water and IPA.

### 2.2 Characterization

The morphology of each step of fabrication was systematically studied by field emission scanning electron microscopy (FESEM, Carl Zeiss). Micro-Raman spectroscopy measurements were carried out using a DILOR-JOBIN-YVON-SPEX integrated Raman spectrometer (Model Labram) with He–Ne 20 mW laser beam as the excitation source. Photoluminescence studies were carried out using spectrofluorometer (Jobin Yvon, Fluorolog—

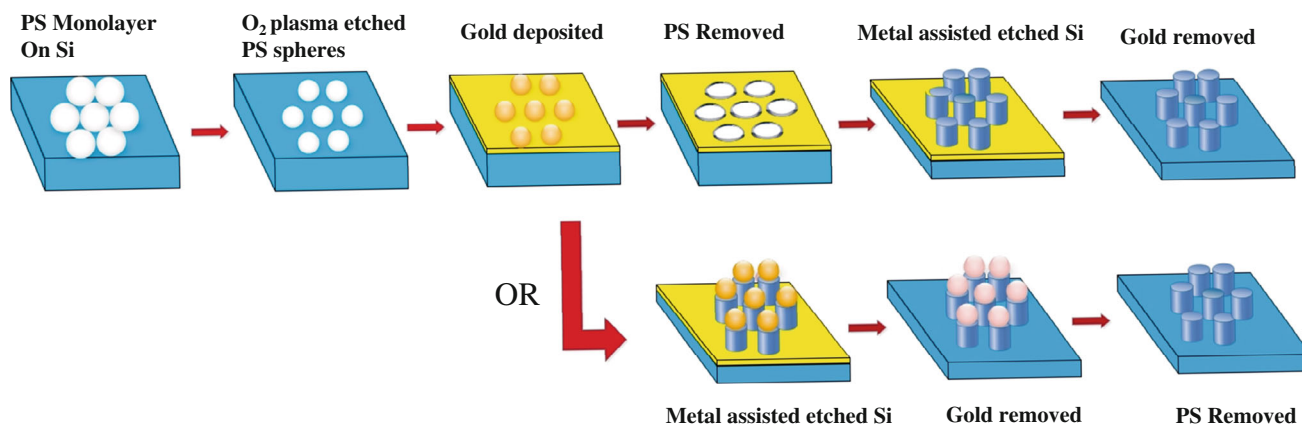


**Fig. 1** Schematic diagram for the fabrication of silicon nanopillars

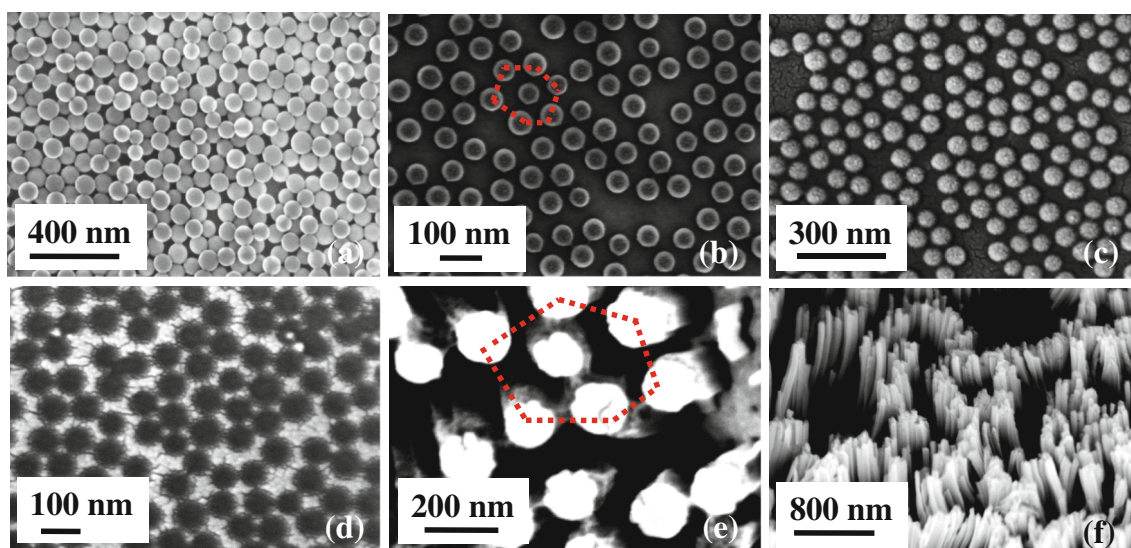


**Fig. 2** FESEM images for PS nanosphere lithography **a** monolayer of PS nanospheres on Si substrate. **b** PS nanosphere separated using O<sub>2</sub> plasma etching. **c** Gold thin film deposited on separated PS

nanospheres. **d** Nanoporous gold template on Si by the after removal of PS nanospheres. **e** Top view of SiNPLs and **f** 20° tilted view of SiNPLs

FL311) with 360 nm as the excitation source. The presence of SiO<sub>2</sub> along with the silicon nanopillars is detected by X-ray photoelectron spectroscopy (XPS-SPECS), using non-monochromatic AlK<sub>α</sub> radiation (1486.8 eV). The binding energies reported here were calculated with reference to C 1s peak at 284.6 eV with a precision of 0.1 eV.

### 3 Results and discussion

#### 3.1 The mechanism and the evolution of surface morphology of Si nanopillars

The surface morphology of each step of fabrication was systematically studied using FESEM and is shown in Fig. 2. Figure 2a–d represents the images for PS

nanosphere lithography, and Fig. 2e, f shows the top and 20° tilted views of the SiNPLs. The arrangement of SiNPLs in hcp structure is clearly visible in Fig. 2e. The FESEM images of PS nanospheres after O<sub>2</sub> plasma etching are shown in Fig. 3. The reduction in size of PS nanospheres and interparticle distance with O<sub>2</sub> plasma etching time are plotted in the inset of Fig. 3. It must be noted that the SiNPLs are individual free standing pillars. The upper part of the SiNPLs can be bundled together for very high aspect ratio pillars. It may be due to the surface tension force exerted on the nanopillars during drying process. The evolution of the surface morphology of the SiNPLs originates from the mechanism of metal-assisted chemical etching. The nanopillars fabricated by metal-assisted chemical etching obviously have a large surface-to-

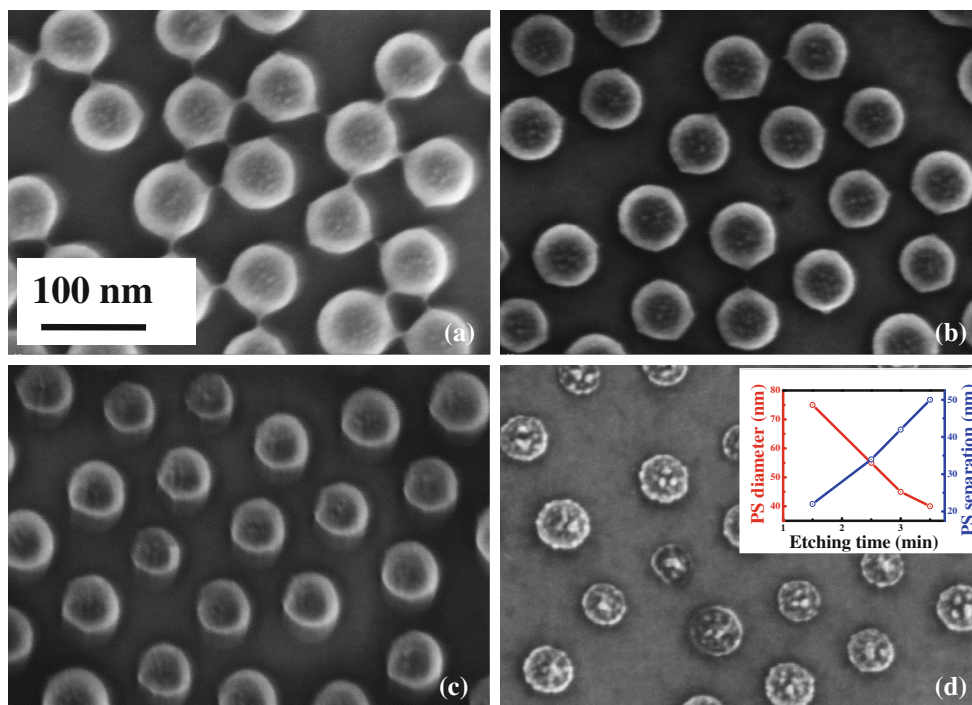
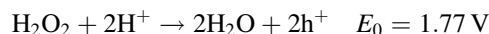


**Fig. 3** FESEM image of PS nanospheres on Si with different O<sub>2</sub> plasma etching time **a** 1 min 30 s **b** 2 **c** 3 **d** 4 min

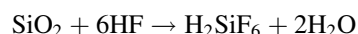
volume ratio when compared to the bulk. The aspect ratio of the SiNPLs is essentially determined by the etching time as the diameter SiNPLs was constant for all the experiments. Hence, we have performed metal-assisted chemical etching with different durations varying from 5 to 20 min and the corresponding cross-sectional FESEM images are shown in Fig. 4. The variation in pillar height with etching time is plotted in inset of Fig. 4, and the height of the pillars varies linearly with the etching time. The etching rate of the SiNPLs depends on the catalyst film morphology, uniformity and the etchant concentration [37]. The average etching rate observed in our SiNPLs is  $\sim 1.15 \mu\text{m}/\text{min}$ . The nanopillars formed by metal-assisted chemical etching can have rough or smooth surfaces depending on the catalyst used for etching. Generally, Ag catalyst produces very rough surfaces due to the secondary etching caused by the diffused Ag layer on the surface of nanopillars. However, on the contrary, Au catalysts are found to be stable against the secondary etching on the nanopillar sidewall to an extent [38].

In the wet chemical fabrication procedure with the presence of Au and H<sub>2</sub>O<sub>2</sub>, oxygen centers could be formed at the dangling surface Si bonds to form SiO<sub>x</sub> [39, 40]. Upon attachment of noble metal film to the Si substrate, the reduction of H<sub>2</sub>O<sub>2</sub> injects holes at the metal surface [40]. The process is analogous to the conventional electrochemical method with noble metal as a microscopic cathode and Si as anode. The schematic diagram for the

mechanism of metal-assisted chemical etching is shown in Fig. 5a. At the cathode, H<sub>2</sub>O<sub>2</sub> from the etching solution gets reduced with the liberation of holes. The protons are reduced to hydrogen in another cathodic reaction [40].



The electrochemical potential of H<sub>2</sub>O<sub>2</sub> is much higher than the valence band energy of Si, thus causing injection of holes into Si. The bubble formation observed during the etching process is probably due to the liberation of hydrogen. Considering the various possible reactions at the anode, the most possible reaction in our case is the formation of SiO<sub>2</sub> accompanied by the dissolution of oxides [41].



Now, we extend our observation to the surface of the individual SiNPLs. The cross-sectional FESEM images for the SiNPLs are shown in Fig. 5b–d. Figure 5d shows that the top portion of the SiNPLs contains highly porous structure, which is believed to be mesoporous structures. On the other hand, the bottom region of the SiNPLs is fairly smooth. The pores at the top region of the SiNPLs originate from the Au-coated PS nanosphere at the top of the nanopillars, which had not been removed. The

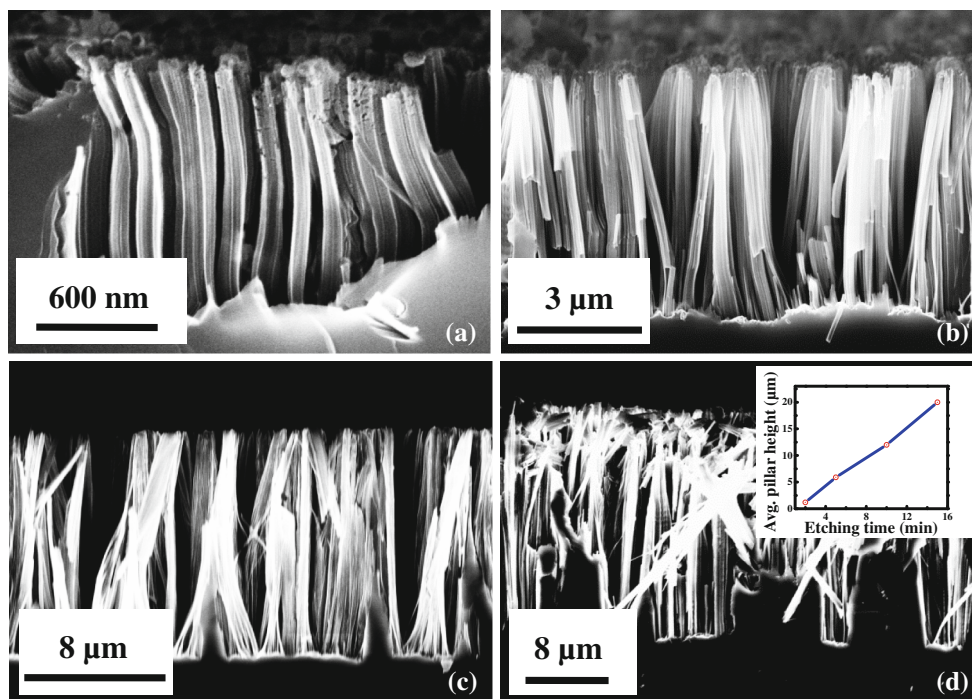


Fig. 4 Cross section of Si nanopillars with different etching times a 2 b 5 c 10 and d 15 min

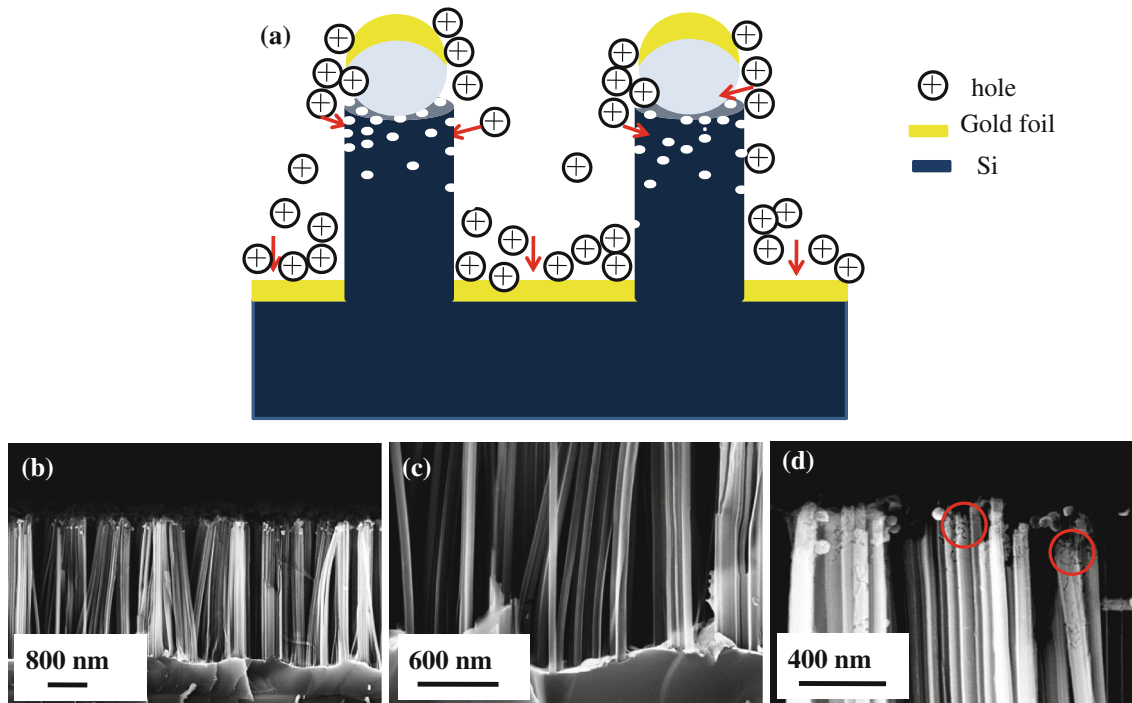


Fig. 5 a Schematic diagram showing the mechanism of metal-assisted chemical etching and the formation of P-SiNCs in SiNPLs. b–d The FESEM cross-sectional images for the SiNPLs. c The bottom

region of the SiNPLs d Top portion of the SiNPLs. The red circle area shows the nanoporous microstructure at the tip of SiNPLs

remaining Au at the tip acts as cathode that catalyzes the reduction of H<sub>2</sub>O<sub>2</sub>. Then the generated holes diffuse to the top of the nanowires and induce the anode reaction. This

must be the reason to observe high porosity at the tip of SiNPLs than the center or the bottom of the SiNPLs. At the same time, the porosity of the other regions of the SiNPLs,

i.e., at the bottom and the middle portion of the Si nanopillars can be due to the lateral sidewall injection of the holes, generated by the reduction of  $\text{H}_2\text{O}_2$  at the cathode, from the etching front to the sidewall of the SiNPLs [41]. So, there is an evolution of silicon nanocrystals, i.e., the exposed regions between two nanoporous structures. Hereafter, we call these silicon nanocrystals on the SiNPLs as porous silicon nanocrystals (*P*-SiNCs). The porosity of the SiNPLs can be tuned by varying the etchant concentration. In order to control the surface roughness and the porosity of the SiNPLs, we have used an etching solution of  $\text{HF}/\text{H}_2\text{O}_2$  in the ratio 3:1. In order to check the dependence of  $\text{H}_2\text{O}_2$  on the porosity of the SiNPLs, the SiNPLs were fabricated with different concentrations of  $\text{H}_2\text{O}_2$  varying from 4 to 7 ml, as shown in Fig. 6. It could be seen from the FESEM images that the porosity of the SiNPLs increases with increase in concentration of  $\text{H}_2\text{O}_2$ . The number density of the holes increases with the increase in  $\text{H}_2\text{O}_2$  concentration, causing the high porosity on the SiNPLs as mentioned before. Solid SiNPLs can be formed by reducing amount of  $\text{H}_2\text{O}_2$  which limits the applications of SiNPLs in luminescent devices due to the absence of porous structure [39].

The porous structure on the SiNPLs can be microporous (<2 nm), mesoporous (<50 nm) or macroporous (<100 nm). In order to find the pore distribution associated with the SiNPLs, we have performed BET gas adsorption analysis.

### 3.1.1 BET gas sorption analysis

The BET gas sorption experiments were performed to investigate the porosity of the SiNPLs formed by metal-assisted chemical etching. The nitrogen adsorption and desorption isotherms of the porous SiNPLs performed at 77 K are plotted in Fig. 7a. Figure 7a exhibits Type IV classification of isotherms with a small hysteresis between adsorption and desorption isotherms [42]. The hysteresis loop associated with the SiNPLs indicates the capillary condensation in porous structures on the SiNPLs. The hysteresis loop can be considered as H3 type by IUPAC classification of hysteresis [42]. According to this classification, the SiNPLs consist of random pores with slit or wedge shaped structures. The pore distribution analysis carried out by non-localized density functional theory (NLDFT) is shown in Fig. 7b. According to this method, the majority of the pore diameters are in the range of 3–15 nm and the most probable pore diameters are 4.4 and 7.1 nm, as shown in Fig. 7b. The pore distribution histogram obtained from the NLDFT analysis is shown in Fig. 7c. The DFT–Monte Carlo cumulative pore volume plot also is shown in Fig. 7d. Figure 7d shows that the pore diameter starts from  $\sim 3$  nm and reaches maximum cumulative pore volume at  $\sim 15$  nm. The desorption branch of the isotherm was taken for the NLDFT analysis as well as BJH analysis. The cumulative surface area, pore volume and pore width obtained by BJH method are  $31.29 \text{ m}^2/\text{g}$ ,  $0.042 \text{ c/g}$  and  $3.61 \text{ nm}$ , respectively.

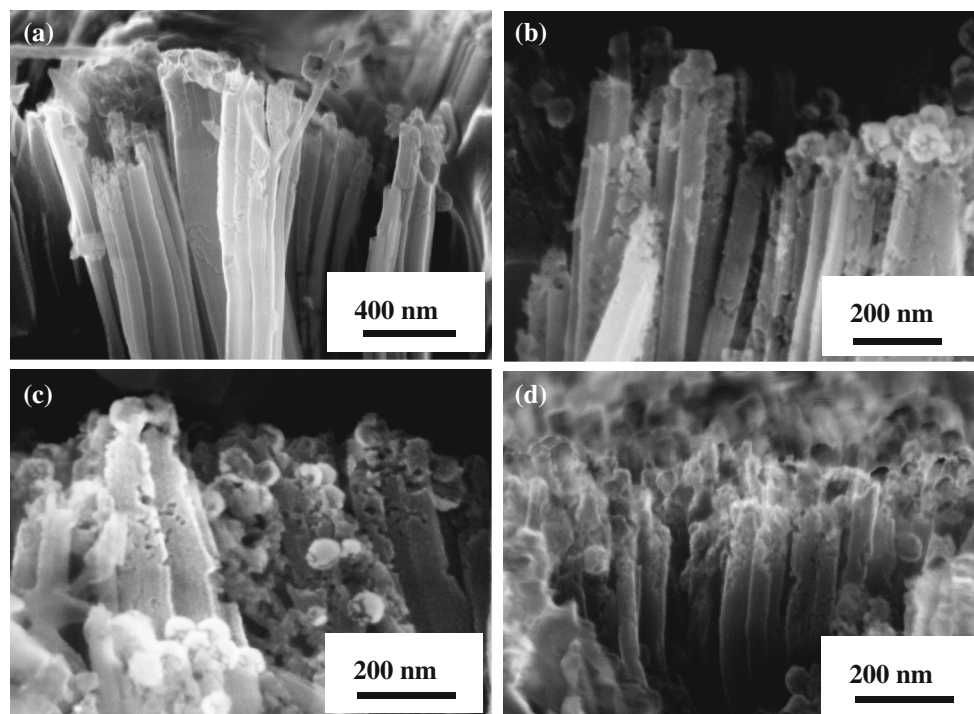
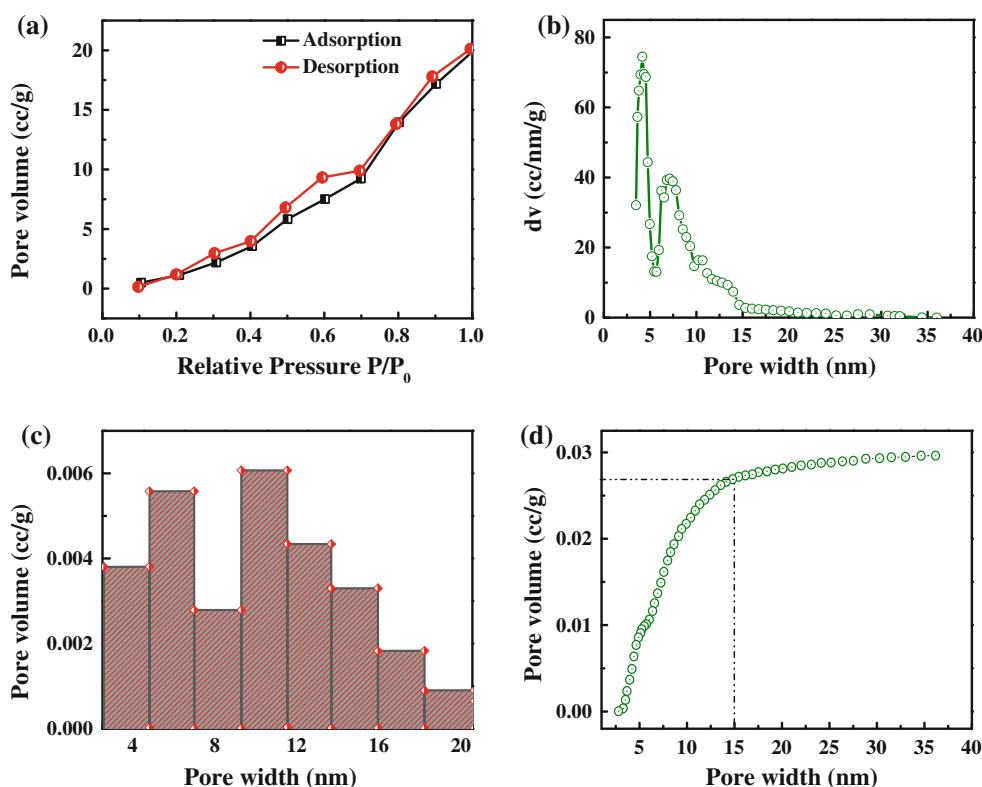


**Fig. 6** FESEM images of SiNPLs formed with different  $\text{H}_2\text{O}_2$  concentrations **a** **b** **c** **d** 7 ml of  $\text{H}_2\text{O}_2$

**Fig. 7** Nitrogen adsorption–desorption isotherm of porous SiNPLs. **b** Differential pore volume–pore width plot. **c** Histogram for the pore distribution of porous SiNPLs. **d** NLDFT–Monte Carlo cumulative pore volume plot for the porous SiNPLs



The mesoporous SiNPLs have additional advantages over the solid silicon nanopillars due to the presence of the mesoporous structures and the P-SiNCs. The porous structures can be employed in electroluminescent devices such as light-emitting diodes and injection lasers [43]. The photoluminescence study of the mesoporous SiNPLs is of great importance since it leads to application in silicon-based optoelectronics. The photoluminescence spectra of mesoporous SiNPLs, their origin and correlation with the micro-Raman spectra, role of porous nanocrystallites in quantum confinement, etc. are discussed in Sect. 3.2.

### 3.2 Correlation of Raman spectra and photoluminescence of mesoporous SiNPLs

In order to find the size of porous SiNCs and the quantum confinement property of mesoporous SiNPLs, micro-Raman spectra were recorded. The laser beam is illuminated parallel to the axis of the SiNPLs, and then, the laser is pointed to the tip of the SiNPLs. The variation in Raman intensity with etching time is plotted in Fig. 8a. The Raman intensity of the SiNPLs increases with the etching time. The Raman peak for the crystalline silicon is located at  $521\text{ cm}^{-1}$ . The Raman spectrum for the sample (i.e., etched for 12 min) can be fitted by using two Lorentzians as shown in inset of Fig. 8a. The peak position of the etched silicon is shifted to  $518\text{ cm}^{-1}$  with an additional

shoulder peak at  $504\text{ cm}^{-1}$ . The optical phonons of the bare crystalline silicon occur at with a phonon momentum  $q = 0$  for Raman process. For the etched silicon due to phonon confinement  $q > 0$ , the optical phonon mode splits into LO and TO modes [44]. The peaks observed at  $518$  and  $504\text{ cm}^{-1}$  correspond to LO and TO phonons, respectively. The finite particle size  $d$  corresponds to a momentum of  $q = \pm \frac{2\pi}{d}$ , which determines the position of Raman peak in the spectra. The Raman frequency shift is given by [44]

$$\Delta\omega = \omega(L) - \omega_0,$$

where  $\omega(L)$  is the Raman frequency of the etched Si with crystallite size  $L$  and  $\omega_0$  is the Raman frequency of bare crystalline Si at  $\Gamma$  point. The Raman frequency shift can be obtained by using the analytic form of bond polarizability model for spherical confinement [44]

$$\Delta\omega = -A\left(\frac{a}{L}\right)^\gamma,$$

where  $\Delta\omega$  is Raman frequency shift observed between bare Si and etched Si,  $A = 47.41$  and  $\gamma = 1.44$  for spherical confinement of the optical phonons. By using this analytic model the average crystallites size in our SiNPLs is of 2–3 nm. The shift in Raman peak and splitting into LO and TO modes provide strong evidence for the existence of 2–3 nm-sized crystallites (shown in Fig. 8b). The spherical confinement of optical phonons and the splitting into LO

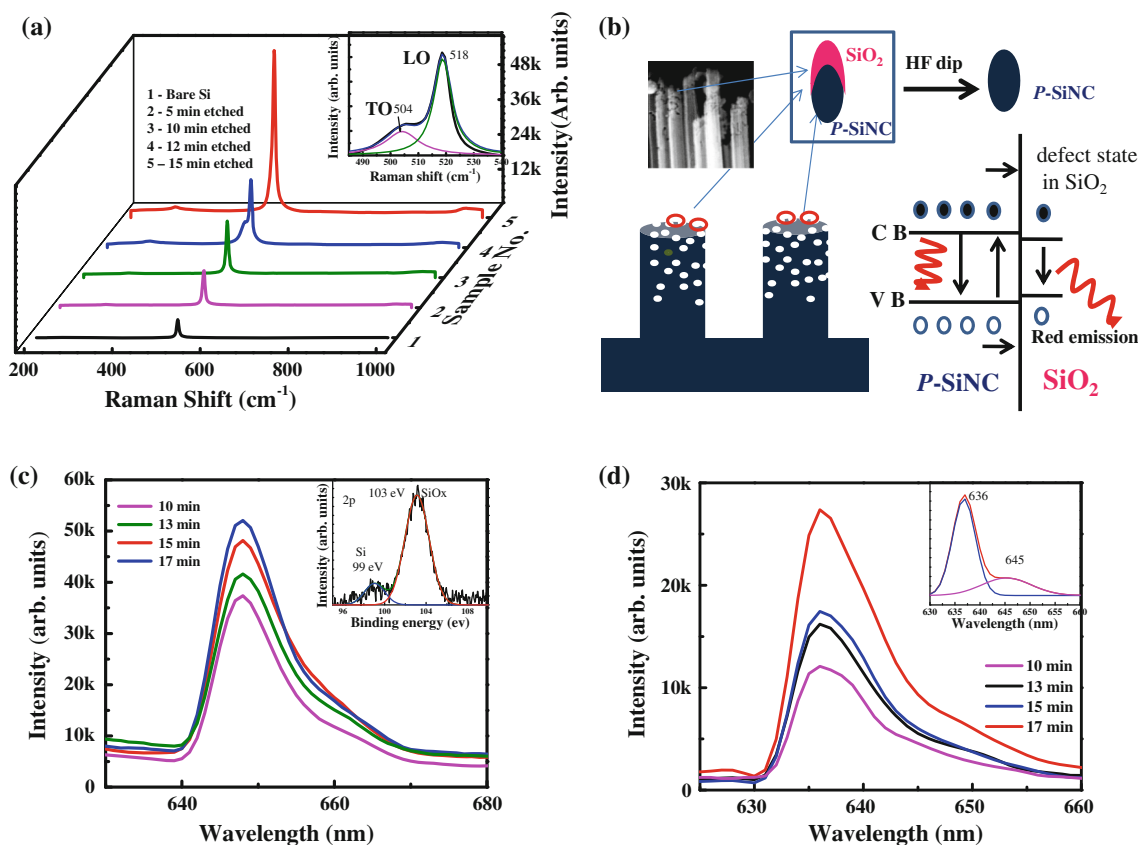


**Fig. 8** **a** Micro-Raman spectra of bare and SiNPLs etched for different durations. Raman spectrum of SiNPLs fitted by using two Lorentzians is shown in *inset*. **b** Schematic diagram shows the structure of *P*-SiNC and the mechanism of photoluminescence of

SiNPLs. **c** Photoluminescence spectra of SiNPLs. *Inset* shows the deconvoluted photoluminescence spectrum. **d** Si 2p XPS spectrum of SiNPLs

and TO is attributed due to the presence of *P*-SiNC on the top of SiNPLs. The evolution of *P*-SiNC in the SiNPLs was discussed earlier. Hence, the splitting of LO and TO phonon modes clearly confirms the quantum confinement property of 2–3 nm *P*-SiNC in SiNPLs, which in turn corroborated with the origin of red luminescence.

The photoluminescence spectra of SiNPLs are shown in Fig. 8c. There is a clear red emission at 647 nm (1.91 eV) with a shoulder peak at 655 nm. The intensity of the peaks increases with the etching time. The origin of the red luminescence could be either due to the recombination of the electron–hole pairs between the quantum-confined electronic levels of the *P*-SiNC or due to the luminescent defect states at the interface region between the Si nanocrystals and SiO<sub>2</sub> [45]. The red emission from our SiNPLs is predominantly due to the quantum confinement property (QC model) of the *P*-SiNC of size 2–3 nm. Meanwhile, the emission at 655 nm could be due to the excitonic transition in the Si nanocrystals [46]. Another explanation is possible for the red emission using quantum confinement luminescence center model (QCLC) [47]. The presence of residual SiO<sub>2</sub>, which is not being

removed by the action of HF during etching, is detected by using XPS. Si 2p XPS spectrum of SiNPLs is shown in inset of Fig. 8c. The characteristic peak of Si–Si bond is centered at a binding energy of 99 eV and SiO<sub>2</sub> peak is centered at 103 eV [48]. Huang et al. [12] have reported the thickness variation of the SiO<sub>2</sub> on SiNPLs fabricated by nanosphere lithography and metal-assisted chemical etching with HRTEM observations. They have reported that thickness of SiO<sub>2</sub> at the tip of the SiNPLs is less than 8 nm and at the bottom region it is less than 2 nm. So, in our case the *P*-SiNC could be partially wrapped up with a few nanometer thickness SiO<sub>2</sub> and it acts like a well-separated Si/SiO<sub>2</sub> quantum dots and the *P*-SiNC/SiO<sub>2</sub> system is schematically represented in Fig. 8b. According to this model, after excitation the carrier can tunnel through the barrier made by SiO<sub>2</sub> and the emission happens through any defect states present in the amorphous SiO<sub>2</sub>. Since we are getting red emission at 647 nm, the defect state in SiO<sub>2</sub> should present at 1.91 eV. Hence, the photo excitation occurs in the *P*-SiNC and the photoemission takes place in the luminescent center in SiO<sub>2</sub> close to Si nanocrystallites [45].



The porous Si nanopillars are highly applicable to LED devices, only if the red emission is from the P-SiNC. In order to find the exact origin of red luminescence, the photoluminescence spectra of SiNPLs were taken after dipping in HF solution. The PL spectra of SiNPLs after HF dip are shown in Fig. 8d. The spectra also show a clear red emission at 636 nm with a shoulder peak at 645 nm. The corresponding band gap of the P-SiNC is 1.94 eV. The red emission of the SiNPLs after HF dip must be from the P-SiNCs, since the SiO<sub>2</sub> native oxide layer is removed by HF. The shift in the PL spectra after HF dip is due to the direct red emission in the P-SiNC (shown in schematic Fig. 8b) by the removal of all the luminescent states present in the amorphous SiO<sub>2</sub> [49]. The decrease in PL intensity before and after HF dip is possibly due to the contribution of SiO<sub>2</sub>-related luminescence. Therefore, we confirmed that the P-SiNCs, evolved during the metal-assisted chemical etching due to the lateral injection of holes, are responsible for the phonon confinement and red photoluminescence. The findings indicate that LED devices can be made in a facile and cost effective method using our mesoporous SiNPLs.

#### 4 Conclusion

We have successfully fabricated vertical SiNPLs of diameter ~80 nm by combining metal-assisted chemical etching and nanosphere lithography. The surface morphology and evolution mechanism of P-SiNC on top of SiNPLs were discussed in detail. We have detected the presence of P-SiNCs on the SiNPLs using FESEM studies and the porosity variation with H<sub>2</sub>O<sub>2</sub> concentration is also examined. The characteristic size of the crystallites was calculated from the micro-Raman spectra using bond polarizability model for spherical confinement. The origin of the red luminescence could be either due to the recombination of electron-hole pairs between the quantum-confined electronic levels of the P-SiNC (QC model) or due to the luminescent defect states at the interface region between the Si nanocrystals and SiO<sub>2</sub> (QCLC model). We have successfully correlated photoluminescence and the Raman spectra observed for mesoporous SiNPLs. Finally, we confirmed the red emission is from the P-SiNCs, which is highly preferable for LED devices.

**Acknowledgments** The authors are thankful to the Director, CSIR-NAL, for his support and encouragement. Mr. G. Srinivas and Mr. Praveen Kumar are thanked for various measurements. Mr. Mariappan is thanked for BET measurements. Mr. Benjamin (Pondicherry University) is thanked for PL measurements. BRNS (Project No.: U-1-125) is thanked for SRF fellowship to K. P.

#### References

1. A.I. Hochbaum, R. Chen, R.D. Delgado, W. Liang, E.C. Garnett, M. Najarian, A. Majumdar, P. Yang, *Nature* **451**, 163–168 (2008)
2. V. Schmidt, H. Riel, S. Senz, S. Karg, W. Riess, U. Gösele, *Small* **2**, 85–88 (2006)
3. B. Tian, X. Zheng, T.J. Kempa, Y. Fang, N. Yu, G. Yu, J. Huang, C.M. Lieber, *Nature* **449**, 885–890 (2007)
4. S.M. Lee, R. Biswas, W. Li, D.O. Kang, L. Chan, J. Yoon, *ACS Nano* **8**, 10507–10512 (2014)
5. K.Q. Peng, S.T. Lee, *Adv. Mater.* **23**, 198–215 (2011)
6. C.K. Chan, H. Peng, G.A.O. Liu, K. Mcilwrath, X.F. Zhang, R.A. Huggins, Y.I. Cui, *Nat. Nanotechnol.* **411**, 31–35 (2007)
7. S.F. Leung, Q. Zhang, F. Xiu, D. Yu, J.C. Ho, D. Li, F.J. Zhiyong, *Phys. Chem. Lett.* **5**, 1479–1495 (2014)
8. H. Yu, X. Duan, C.M. Lieber, *Small* **1**, 142–147 (2005)
9. S.W. Chang, J. Oh, S.T. Boles, C.V. Thompson, *Appl. Phys. Lett.* **96**, 153108 (2010)
10. Y. Cui, Q. Wei, H. Park, C.M. Lieber, *Science* **293**, 1289–1292 (2001)
11. W. Xu, C.S. Ozkan, *Nano Lett.* **8**, 398–404 (2008)
12. Z.P. Huang, N. Geyer, P. Werner, J.D. Boor, U. Gosele, *Adv. Mater.* **23**, 285–308 (2011)
13. B. Kiraly, S. Yang, T. Huang, *J. Nanotechnol.* **24**, 245704–245705 (2013)
14. X. Zhao, C.M. Wei, L. Yang, M.Y. Chou, *Phys. Rev. Lett.* **92**, 236805 (2004)
15. R. Ghosh, P.K. Giri, K. Imakita, M. Fujii, *Nanotechnology* **25**, 045703–045705 (2014)
16. L.A. Osminkina, K.A. Gonchar, V.S. Marshov, K.V. Bunkov, D.V. Petrov, L.A. Golovan, F. Talkenberg, V.A. Sivakov, V.U. Timoshenko, *Nanoscale Res. Lett.* **7**, 524–528 (2012)
17. V. Gowrishankar, S.R. Scully, A.T. Chan, M.D. McGehee, Q. Wang, H.M.J. Branz, *Appl. Phys.* **103**, 064511 (2008)
18. J. Goldberger, A.I. Hochbaum, R. Fan, P. Yang, *Nano Lett.* **6**, 973–977 (2006)
19. H. Schmid, M.T. Bjork, J. Knoch, H. Riel, W. Riess, P. Rice, T. Topuria, *J. Appl. Phys.* **103**, 024304–024306 (2008)
20. D. Shakhiveli, S.J. Raghavan, *Appl. Phys.* **112**, 024317–024322 (2012)
21. Y. Wang, V. Schmidt, S. Senz, U. Gosele, *Nat. Nanotechnol.* **1**, 186–189 (2006)
22. S. Hofmann, R. Sharma, C.T. Wirth, S.F. Cervantes, C. Ducati, T. Kasama, R.E. Dunin-Borkowski, J. Drucker, P. Bennett, J. Robertson, *Nat. Mater.* **7**, 372–375 (2008)
23. K. Omar, Y. Al-Douri, A. Ramizy, Z. Hassan, *Superlattices Microst.* **50**, 119–127 (2011)
24. Z. Huang, H. Fang, J. Zhu, *Adv. Mater.* **19**, 744–748 (2007)
25. C.L. Cheung, R.J. Nikolic, C.E. Reinhardt, T.F. Wang, *Nanotechnology* **17**, 1339–1343 (2006)
26. A.V. Whitney, B.D. Myers, R.P. Van Duyne, *Nano Lett.* **4**, 1507–1511 (2004)
27. R. Liu, F. Zhang, C. Con, B. Cui, B. Sun, *Nanoscale Res. Lett.* **8**, 155–163 (2013)
28. K.Q. Peng, Y.J. Yan, S.P. Gao, J. Zhu, *Adv. Mater.* **14**, 1164–1168 (2002)
29. K.Q. Peng, Y.J. Yan, S.P. Gao, J. Zhu, *Adv. Funct. Mater.* **13**, 127–132 (2003)
30. K.Q. Peng, Z.P. Huang, J. Zhu, *Adv. Mater.* **16**, 73–76 (2004)
31. K.Q. Peng, Y. Wu, H. Fang, X.Y. Zhong, Y. Xu, J. Zhu, *Angew. Chem. Int. Ed.* **44**, 2797–2802 (2005)
32. K.Q. Peng, H. Fang, J.J. Hu, Y. Wu, J. Zhu, Y.J. Yan, S. Lee, *Chem. Eur. J.* **12**, 7942–7947 (2006)
33. K.Q. Peng, J.J. Hu, Y.J. Yan, Y. Wu, H. Fang, Y. Xu, S.T. Lee, J. Zhu, *Adv. Funct. Mater.* **16**, 387–394 (2006)

34. W.K. Choi, T.H. Liew, M.K. Dawood, H.I. Smith, C.V. Thompson, M.H. Hong, *Nano Lett.* **8**, 3799–3802 (2008)
35. F. Demami, L. Pichon, R. Roger, A.C. Salaun, *Mater. Sci. Eng.* **6**, 012014–012019 (2009)
36. Z.P. Huang, Y. Wu, H. Fang, J. Zhu, *Nanotechnology* **17**, 3768–3774 (2006)
37. X. Li, *Curr. Opin. Solid State Mater. Sci.* **16**, 71–81 (2012)
38. W. Chem, K. Hsu, I. Chun, B.P. de Azeredo, N. Ahmed, K.H. Kim, *Nano Lett.* **10**, 1582–1588 (2010)
39. Z.P. Huang, X.X. Zhang, M. Reiche, L.F. Liu, W. Lee, T. Shimizu, S. Senz, U. Gosele, *Nano Lett.* **8**, 3046–3051 (2008)
40. S.W. Chang, V.P. Chuang, S.T. Boles, C.A. Ross, C.V. Thompson, *Adv. Funct. Mater.* **19**, 2495–2500 (2009)
41. C. Chartier, S. Bastide, C. Levy-Clement, *Electrochim. Acta* **53**, 5509–5516 (2008)
42. A.A.S.M. Radzi, S.F.M. Yusop, M. Rusop, Abdullah, *Mat. Sci. Eng. R* **40**, 012046–012052 (2012)
43. G.R. Lina, C.J. Lin, H.C. Kuo, *Appl. Phys. Lett.* **91**, 093122–093123 (2007)
44. R. Tsu, H. Shen, M. Dutta, *Appl. Phys. Lett.* **60**, 112–114 (1992)
45. J. Zi, K. Zhang, X. Xie, *Phys. Rev. B* **55**, 15–21 (1997)
46. J. Heitmann, F. Muller, L. Yi, M. Zacharias, *Phys. Rev. B* **69**, 195309 (2004)
47. G.G. Qin, Y.J. Li, *Phys. Rev. B* **68**, 085309 (2003)
48. R. Alfonsetti, L. Lozzi, M. Passacantando, P. Piccuzzi, S. Santucci, *Appl. Surf. Sci.* **70**, 222–227 (1993)
49. P. Kumar, *ISRN Nanotechnol.* **2011**, 163168 (2011)